Structure-Transport Relationships in Disordered Solids Using Integrated Rate of Gas Sorption and Mercury Porosimetry

Artjom Nepryahin[a], Elizabeth M. Holt[b], Rob S. Fletcher[b] and Sean P. Rigby[a]

[a]Department of Chemical and Environmental Engineering, University of Nottingham, University Park, Nottingham NG7 2RD, United Kingdom

[b] Johnson Matthey, P.O. Box 1, Belasis Avenue, Billingham, Cleveland, TS23 1LB, United Kingdom

*Corresponding author

Current address: Department of Chemical and Environmental Engineering, University of Nottingham, U.K.

Telephone No.: +44 (0) 115 951 4078

Email: enzspr@exmail.nottingham.ac.uk

Abstract

This work describes a new experimental approach that delivers novel information on structure-transport relationships in disordered porous pellets. Integrated rate of adsorption and mercury porosimetry experiments have been used to probe the relative importance of particular sub-sets of pores to mass transport rates within the network of two disordered porous solids. This was achieved by examining the relative rates of low pressure gas uptake into a network, both before, and after, a known set of pores was filled with frozen, entrapped mercury. For catalyst pellets, formed by tableting, it has been found that the compaction pressure affects the relative contribution to overall mass transport made by the subset of the largest pores. Computerised X-ray tomography (CXT) has been used to map the spatial distribution of entrapped mercury and revealed that the relative importance of the sub-sets of pores is related to their level of pervasiveness across the pellet, and whether they percolate to the centre of the pellet. It has been shown that a combination of integrated mercury porosimetry and gas sorption, together with CXT, can comprehensively reveal the impact of manufacturing process parameters on pellet structure and mass transport properties. Hence, the new method can be used in the design and optimisation of pellet manufacturing processes.

Keywords: catalyst pellet; effectiveness factor; pore diffusion; X-ray imaging; pore characterization

INTRODUCTION

Disordered porous solids with complex void space structures are still commonly used as catalyst supports, adsorbents, and chromatographic media. This is because more ordered, controlled pore size materials are often hydrothermally unstable and/or expensive. The complex pore network structure of amorphous materials makes understanding the particular performance of these materials difficult. For many industrial processes, involving porous heterogeneous catalysts, the effectiveness factor of the pellets is well below one hundred percent, due to diffusion limitations. For example, typical effectiveness factors for industrial processes are often only ~50-60%. Poor pellet effectiveness is caused by high diffusional resistance reducing pellet mass transfer rates. Many industrial processes operate under temperature and pressure conditions such that pore diffusion occurs in the Knudsen regime where the size of the diffusivity is proportional to the pore size. In such circumstances, to lower diffusional resistance, pervasive networks of large pore 'motorways' are often introduced into the pellet to provide better access to the centre of the pellet where there are more smaller pore 'side-roads' providing active surface area. Increased numbers of larger pores can also increase resistance to deactivation by solids deposition, such as coking. However, the surface-to-volume ratio of larger pores is lower than that of small pores, and hence adding more large pores to aid diffusion means the active surface area per unit pore volume is reduced leading to a decline in specific activity. Further, the presence of any large pores provides weak points that can reduce pellet strength and compromise structural integrity. There is thus an optimum combination of large and small pores for a given reaction. Even for disordered materials there is some potential to control structural characteristics such as porosity, modal pore sizes, and width of the distribution(s).

The existence of this compromise in catalyst pellet design has led many workers to try to use computer simulation to understand catalyst performance and determine the optimum pore structure for a given reaction. However, even today, available computing power places limits on the volume of a real catalyst that it is possible to represent on a computer, and, given a typical, real heterogeneous catalyst pellet contains $>10^{14}$ pores, it is insufficient to represent a single whole catalyst pellet, let alone a full bed. In order to get around this issue it is generally assumed that the pore structure of the catalyst is homogeneous over length-scales

larger than the size of the region simulated. However, magnetic resonance imaging (MRI) (Hollewand and Gladden, 1993; Pavlovskaya *et al.*, 2015) and computerised X-ray tomography (CXT) (Hyväluoma *et al*., 2004; Rigby *et al.*, 2011) studies have shown that typical catalyst pellets have macroscopic (>10 μm) heterogeneities in the spatial distribution of porosity, pore size, and connectivity. Hence, given the limited sample volumes of the pore space that it is possible to image directly using electron tomography (3D-TEM) (Koster *et al*., 2000), dual-beam microscopy (Holzer *et al*., 2004), or synchrotron CXT (Hyväluoma *et al*., 2004), these imaged regions are likely to be statistically unrepresentative of the whole sample volume. Therefore, there is a problem in determining the particular influence that a specific part, or aspect, of the pore structure has on mass transport overall if one is forced to model the entire system. An alternative approach, taken in this work, is to develop experimental methods for directly (i.e. without mediating structural modelling) 'filtering out' those aspects of the real pore structure that have the most influence on mass transport.

MRI can be used to obtain structure-transport relationship information by using a combination of relaxation time contrast and pulsed-field gradient (PFG) contrast images (Hollewand and Gladden, 1993, 1995). The relaxation time contrasted imaging provides spatially-resolved maps of porosity and pore size, while the PFG contrasted images provide spatially-resolved maps of self-diffusivity. However, the pore size maps can only be obtained for chemically-homogeneous materials, such as pure catalyst supports, and the pore size probed is only a local volume-weighted average for the whole image voxel. The PFG diffusivity maps are for molecular diffusion. This work will present a method that can be used for chemically heterogeneous samples, such as supported metal and mixed oxide catalysts, and that provides maps of the pore size distribution, and will consider Knudsen diffusion. MRI combined with cryoporometry (Strange and Webber, 1997) or adsorption (Hitchcock *et al.*, 2010) can provide spatially-resolved pore size distributions but these methods are heavily affected by pore-pore co-operative effects that skew pore size distributions to smaller sizes (Hitchcock *et al.*, 2011, 2014).

The problem with indirect structural characterization methods that can provide statistically representative information for disordered porous solids is that the data thus obtained is necessarily a composite of the information for all parts of the pores space. The advantage of

ordered materials is that, in principle, a given region of the void space should behave the same as all other regions, but this is usually not the case for disordered materials. However, the same clarity, as for ordered materials, could be provided for disordered materials, if the information for particular components of the pore network could be deconvolved from the overall composite signal. Scanning curves are a technique for characterization methods that, in principle, isolates the behaviour of a class of pores of a narrow range in size. However, using scanning curves to isolate the behaviour of a sub-set of pores assumes that there is a monotonic relationship between the control variable (pressure for gas sorption and mercury porosimetry, and temperature for thermoporometry) and pore size, and that the thermodynamic history of the sample does not matter. Hence, using a narrow range of control variable does not necessarily mean probing a narrow range of pore sizes. It is thus difficult to distinguish exactly which pores are being probed by scanning curves.

An alternative approach for studying gas uptake in just subsets of the overall accessible void space involves the co-adsorption of two different adsorbates in series (Gopinathan *et al.*, 2013). For example, a nitrogen sorption experiment is first performed on a dry sample, and then water is adsorbed at a relative humidity that results in partial saturation of the void space, and then that condensed water is frozen in place. A second nitrogen sorption experiment is then performed on the partially ice-filled sample. For most materials, water generally condenses in pores of increasing size with increasing relative humidity, and thus increasing the ultimate humidity in the middle step progressively eliminates ever larger pores from the accessible network. However, since most catalyst materials studied are at least partially water-wetting, the remaining larger pores also often have a multilayer film of significant thickness, or ganglia of substantial size. Hence, in that case, it is necessary to independently know where the water adsorbs in order to unambiguously interpret the nitrogen uptake data. However, the serial adsorption experiment has been used to study water sorption in silicas (Giacobbe *et al.*, 1972), and to probe percolation properties in templated materials (Morishige and Kanzaki, 2009).

A more definitive approach involves the recently developed integrated gas sorption and mercury porosimetry experiment, which uses mercury to block selected subsets of the pore network. Since mercury is non-wetting there are no complicating issues from wetting films,

as with co-adsorption experiments. The integrated method involves running a series of gas sorption and porosimetry experiments on the same sample, freezing in place any mercury that becomes entrapped. The impact on the gas sorption behaviour of the sample due to the replacement of a particular part of the void space with entrapped mercury can be obtained by subtraction. This typically amounts to the sorption isotherms for the subset of pores filled with mercury (Rigby *et al.*, 2004), but, depending on the wetting properties of the adsorbate, can also influence the sorption processes in the empty remainder of the void space (Hitchcock *et al.*, 2015). Further, CXT can be used to determine the spatial location of the particular pores under study in this way because the entrapped mercury is clearly visible in the images. Previous work has considered the impact of the loss of a particular sub-set of pores on the equilibrium sorption behaviour of the network. However, in this work, the impact of the lost pores on mass transport during the kinetic uptake of a gas will be studied.

The new kinetic version of the integrated gas sorption mercury porosimetry experiment described here will enable the particular influence of identifiable sub-sets of pores on the mass transfer within a porous pellet to be determined. Hence, it will be shown how the method can be used to assess the importance of particular pore network features to mass transport. The new technique will be applied to a case study of the influence of the degree of final densification (on two levels, high and low) of a tablet, made with pre-compacted feed particles.

METHOD

2.1 Materials

The materials studied in this work are copper/zinc oxide alumina roll-compacted feed pelleted to form either low density (LD) or high density (HD), cylindrical tablets.

2.2 Integrated mercury porosimetry and gas sorption

Approximately 0.2g of the sample was weighed and placed in a large sample tube made for the gas adsorption rig. The sample tube was then heated to 140 $^{\circ}$C while the sample was under vacuum for a minimum of two hours. The aim of this was to create a standard reference starting point, and to remove any physisorbed substances on the pore surface of the pellet. The sample tube and dry sample were weighed to obtain the mass, and transferred to the Micromeritics ASAP 2010C physisorption rig. The next step was to cool the sample tube to liquid nitrogen temperature by manually raising the Dewar, allowing the sample to freeze for approximately thirty minutes and then the system was evacuated to remove any physisorbed substances. The rate of adsorption was measured using the constant volume method employing the relevant Micromeritics ASAP 2010C software. Sample weights were measured to 3 dp. The instrument was calibrated on an annual basis and weekly instrument performance checks are carried out using the NPL Certified Reference Material M11-02 (Vulcan 3-G (2700) Graphitised Carbon Black Sample Number 2A/8/E/14 having a specific surface area of 71.3 m^2 g^{-1}. A standard physisorption sample tube was used having an overall length of 265 mm; a shaft length of 240 mm; an internal diameter of 9 mm; and a 25 mm diameter bulb. The free space within the tube was minimised by using a solid glass rod with a diameter slightly less than the internal diameter of the tube and about 240 mm long. Nitrogen purity was 99.995%. Isotherms were measured at liquid nitrogen temperature. The isotherms consisted of approximately 60 adsorption points and 40 desorption points. The relative pressure (P_o) was measured for each data point on the isotherm. The absolute pressure tolerance was set at 2.00 mmHg and the relative pressure tolerance was set at 2.0%. The dosing volume for the ROA measurements was typically 5 cc higher than that required to form a monolayer coverage (as taken from BET i.e. V_m) on the sample surface. The 5 cc additional volume was to compensate for the initial expansion of the gas into the free space of the sample tube. The number of readings of pressure vs. time was set at 1000 readings per dose.

Once the initial rate of adsorption experiment was finished, mercury was entrapped in the macropore network by performing a standard mercury intrusion/extrusion experiment reaching the desired intrusion pressure for the level of mercury entrapment. The instrument used was a Micromeritics AutoPore IV 9520 mercury porosimeter. Samples were weighed to

3 dp. The instrument was calibrated on an annual basis and monthly performance checks carried out using the vendors silica-alumina reference material. Triply distilled mercury was used. The mercury intrusion curve consisted of 152 intrusion points from 0.5 psia (0.0034 MPa) to 60000 psia (413.7 MPa) and 100 extrusion points from 60000 psia (413.7 MPa) to 15 psia (0.112 MPa). An equilibration time of 15 seconds was used for each data point. The sample was then transferred back to the Micromeritics ASAP 2010C physisorption rig, where the rate of adsorption experiment was repeated. The sample was cooled to 77K by manually raising the Dewar flask, allowing the sample to freeze for approximately 30 minutes. This part was important in the post mercury entrapment step since it freezes the mercury in-place to ensure that it all remains immobilised within the pellets. The rate of adsorption data was then acquired in the same way as before the mercury entrapment.

The pore size distributions were obtained from the nitrogen adsorption isotherms using the method of Barrett *et al.* (1951), and the *t*-layer correction of Harkins and Jura. A cylindrical-sleeve type geometry was assumed for the meniscus in the Kelvin-Cohan equation, and the adsorbate property factor was 0.953 nm. Pore sizes were obtained from the mercury intrusion curve using the independently-calibrated Kloubek (1981) correlations.

2.3 Computerised X-ray tomography (CXT)

The sample following mercury porosimetry was imaged using a High Resolution X-ray 3D Computed Tomography Microscope Instrument of model VeraXRM-510 (manufactured by Xradia Inc, Pleasanton, CA, USA). The voxel resolution was 6 μm. Typically 2-3 pellets of each sample type were imaged.

THEORY

Rate of adsorption

The mass transfer coefficients were extracted from experiments involving a coupled diffusion and adsorption process. This section outlines the basic theory used to derive a mass transfer coefficient value. When diffusion within a porous solid is accompanied by adsorption, a simple mass balance shows that the usual diffusion equation (here for a sphere with radial co-ordinate r) must be modified to allow for this:

$$\frac{\partial C}{\partial t} = \frac{D_e}{(H+1)}\left[\frac{\partial^2 C}{\partial r^2} + \frac{2}{r}\frac{\partial C}{\partial r}\right], \qquad (1)$$

where D_e is the (purely mass transport) diffusivity, and H is the constant of proportionality between the concentrations of the adsorbed phase and the freely diffusing phase. If there is a linear relationship between the concentrations of the surface adsorbed phase and the freely diffusing phase then solutions of the diffusion with adsorption problem, for given initial and boundary conditions, are the same as for the corresponding problem in simple diffusion except that the modified diffusion coefficient $D_e/(H+1)$ is used. The assumption of a linear relationship between the concentrations of the adsorbate in the gas phase and adsorbed phase only applies over a limited pressure range beyond the Henry's law region. Ideally, a plot of concentration of adsorbed phase against concentration in the gas phase would be acquired using very tiny pressure steps over which the assumption of linearity would be most accurate, but, in order to improve the signal-to-noise ratio in the data, larger pressure steps are necessarily used. The value of H was obtained from using a straight line fit to the isotherm data for the particular pressure step analysed for uptake rate and the two pressure points either side, provided there was insignificant variation in temperature amongst these three pressure points. The lack of significant temperature effects was suggested by the lack of change in overall isotherm shape with the size of the adsorption step chosen (and hence total amount of heat of adsorption released in any one step). The particular uptake data used in this work are for the lowest pressure points in the isotherm. This was to ensure that the surface-adsorbed amount was still very low (~monolayer) and thus did not interfere with the pore diffusion by occupying a significant fraction of the pore wall or cross-section. This also

meant that the diffusion was in the Knudsen regime. This is also the most useful diffusion regime to do the experiments since, when the pellets are used in reactors, the process conditions are such that they typically correspond to Knudsen regime conditions.

The gas uptake data were fitted to a range of equations, including the Linear Driving Force (LDF) model, and spherical and cylindrical geometry solutions to the diffusion equation with well-mixed and constant volume boundary conditions (Crank, 1975). For mass-uptake experiments the appropriate solution to the diffusion equation can often be approximated by the so-called Linear Driving Force (LDF) model and uptake data fitted to the expression (Do, 1998):

$$\frac{M(t)}{M(\infty)} = 1 - \exp(-kt) \tag{2}$$

where k is a mass transfer coefficient (MTC)

For a cylinder submerged in a 'well stirred' reservoir, the appropriate solution to the diffusion equation implies the rate of uptake at time t, can be described by:

$$\frac{M_t}{M_\infty} = 1 - \sum_{n=1}^{\infty} \frac{4\alpha(1+\alpha)}{4+4\alpha+a^2 q_n^2} exp(-Dq_n^2 t/a^2) \tag{3}$$

where q_n are positive non-zero roots of:

$$\alpha q_n J_o(q_n) + 2J_1(q_n) = 0 \tag{4}$$

For a sphere submerged in a 'well stirred' reservoir, the rate of uptake at time t, can be described by:

$$\frac{M_t}{M_\infty} = 1 - \sum_{n=1}^{\infty} \frac{6\alpha(1+\alpha)}{9+9\alpha+a^2 q_n^2} exp(-Dq_n^2 t/a^2) \tag{5}$$

where q_n are positive non-zero roots of:

$$\tan q_n = \frac{3q_n}{3+\alpha q_n^2} \quad (6)$$

Examples of the fits of these equations to a typical set of experimental data are given in Figure 1. As in Figure 1(a), it was found that the cylindrical geometry solution for constant volume gave the best fit, as might have been anticipated from the experimental set-up and apparatus described above. In particular, it can be seen from Figure 1(b) that the cylindrical solution still gives the best fit even at short times. From Figure 1(c) it can be seen that following mercury entrapment the rate of uptake declined but the curve had a similar shape. The fitting parameter obtained was *k*, the mass transfer coefficient (mtc), which is proportional to D_e/a^2 for pure diffusion, where *a* is the effective characteristic particle size. The effective characteristic particle size refers to the maximum straight-line penetration depth that a molecule can access from the exterior, rather the actual tortuous route followed by the diffusive flux. If, for example, the central 'core' region of the sample was non-porous, or encircled by an impermeable boundary, then the effective characteristic particle size would only be the depth of the remaining 'mantle' region still remaining accessible from the exterior. Hence, following entrapment of mercury, it is possible for the mtc to, either increase due to decreased effective characteristic particle size, or decrease due to decreased porosity and increased tortuosity of the remaining void space. The goodness of fit of the cylindrical geometry solution was maintained following entrapment of mercury. The errors in the fitted mtc remained the same, or less, in relative size than that for the fresh samples.

Figure 1: Comparisons, at (a) long times and (b) short times, of the experimental rate of nitrogen uptake for a fresh LD sample (blue line), to the solutions to the diffusion equation for a cylinder in a stirred reservoir of limited volume (red dashes), or a sphere in a stirred reservoir of limited volume (black dash-dot), and also to the LDF model (green dots). Also shown is a comparison (c) of the rate of gas uptake in the LD sample before mercury entrapment (black dashed line) and after mercury entrapment (red solid line) in pores that are greater than or equal to 50nm diameter.

(a)

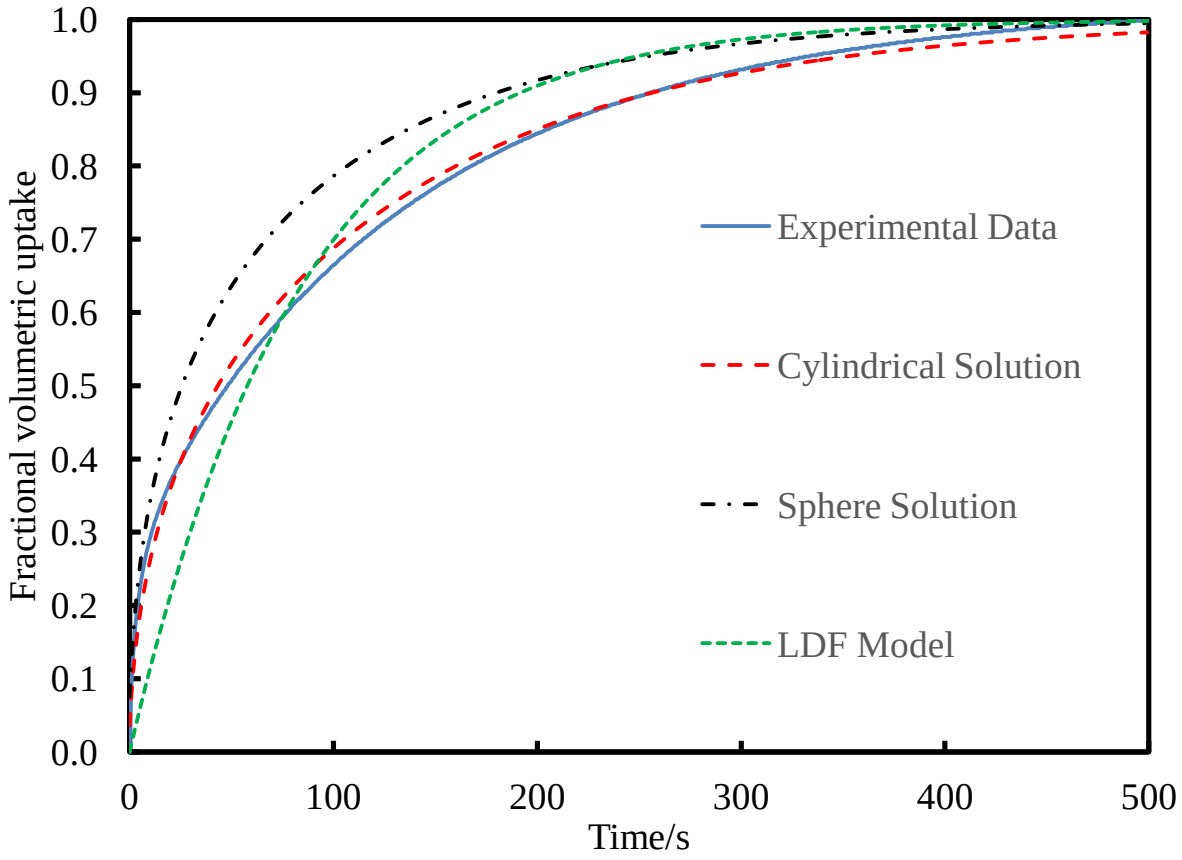

(b)

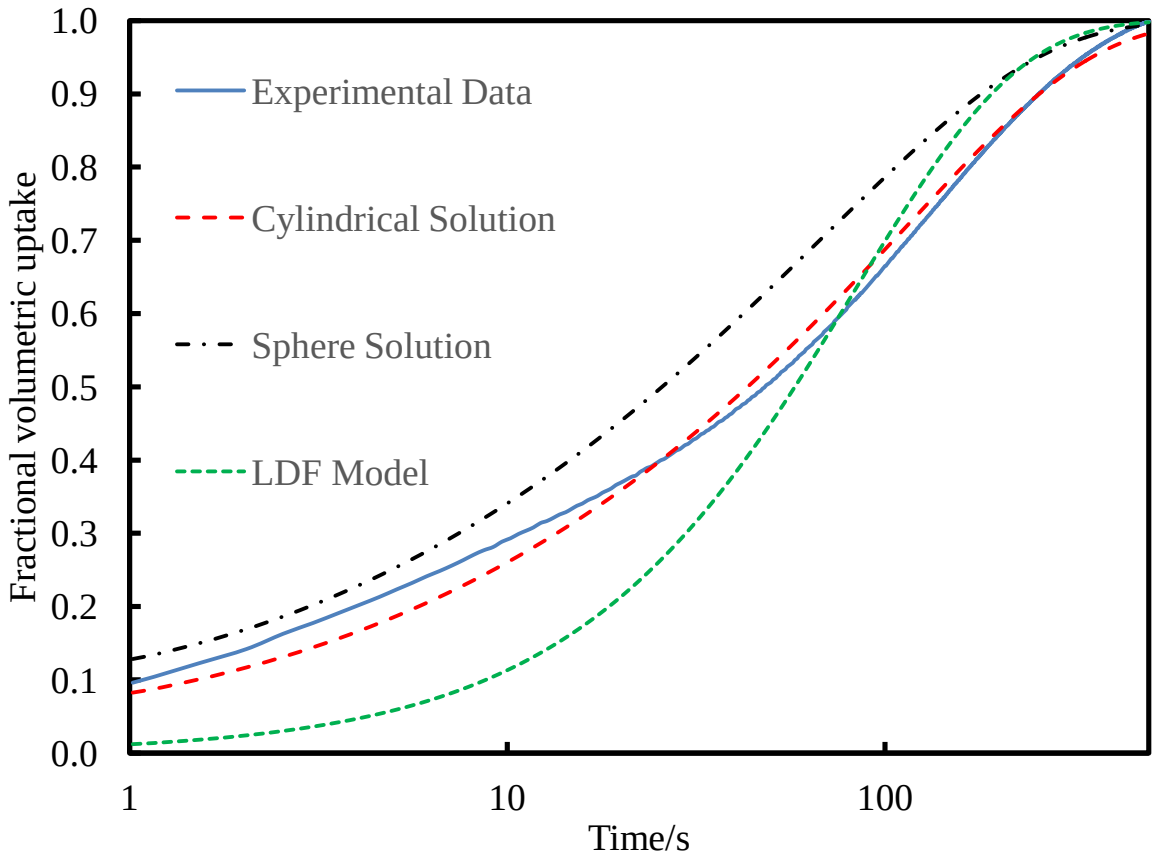
Experimental Data
Cylindrical Solution
Sphere Solution
LDF Model
Fractional volumetric uptake
1.0
0.9
0.8
0.7
0.6
0.5
0.4
0.3
0.2
0.1
0.0
1
10
100
Time/s

(c)

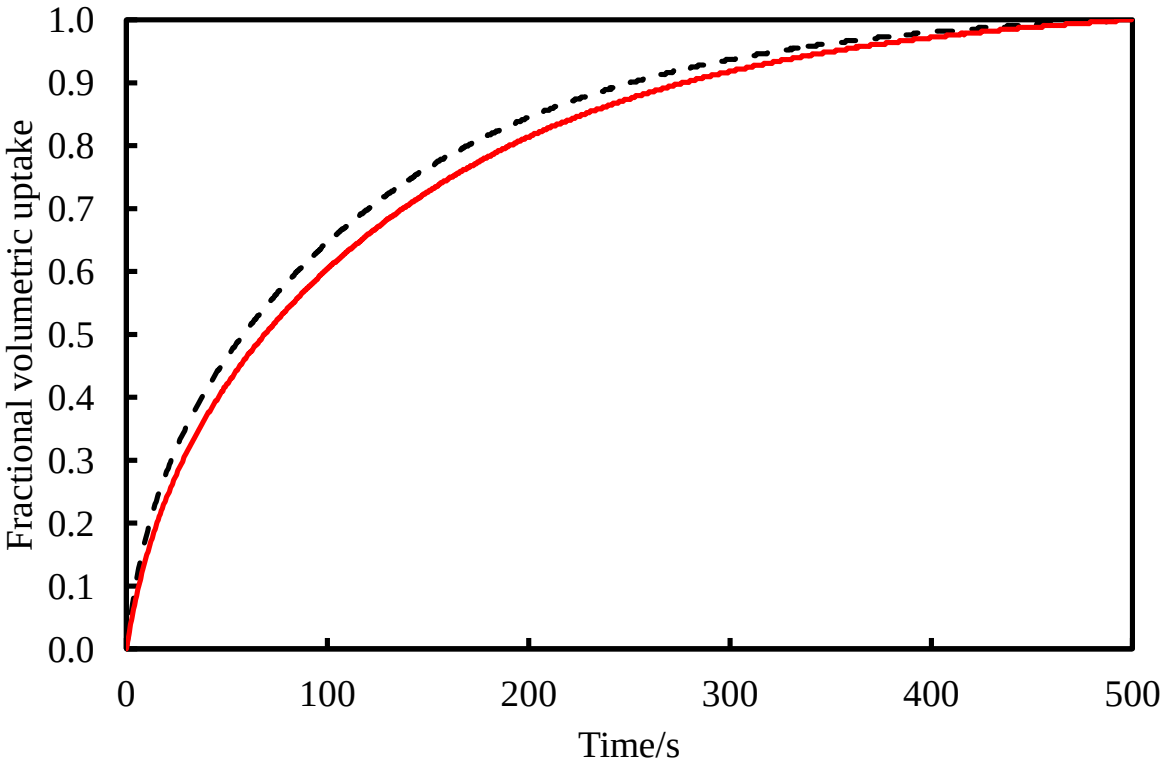
Fractional volumetric uptake
1.0
0.9
0.8
0.7
0.6
0.5
0.4
0.3
0.2
0.1
0.0
0
100
200
300
400
500
Time/s

Benchmark mass transport model

In order to make an assessment of the relative contributions of a given sub-set of pores within the void-space network to mass transport, their transport effectiveness was compared with a 'benchmark' system. Given that, in diffusion modelling, it is typically assumed that catalyst pellets are homogeneous over large length-scales, due to a random distribution of diffusional resistances over shorter length-scales, then a random model system seems the appropriate comparison to make for real systems. As will be seen below, the entrapment of mercury, in the materials studied here, predominantly occurs heterogeneously over macroscopic length-scales, with entrapped mercury generally confined to discrete, spatially-extensive regions, rather than being more pervasively dispersed, as might arise if entrapment varied pore-to-pore between neighbouring pores. The pattern of mercury entrapment is similar to that observed, in glass micromodels with non-random heterogeneity, by Wardlaw and McKellar (1981). Hence, given the importance of macroscopic structural features in determining entrapment, it also seems appropriate to select a benchmark model that represents such patchwise, macroscopic heterogeneity. From a statistical treatment of permeability in heterogeneous media, Prager (1960) proposed a model for the overall diffusivity for a system consisting of disconnected regions of one phase, possessing one value of diffusivity, dispersed amongst a continuum of a second phase with a different diffusivity. In the case of the samples studied here, the dispersed phase will have zero diffusivity because it will correspond to void-space regions containing entrapped mercury, which are typically isolated within seas of smaller, shielding pores. The expression for the expected relative decrease in overall diffusivity is given by:

$$\frac{Observed\ diffusivity}{Original\ diffusivity} = \frac{v_B(v_A+v_B lnv_B)}{2(v_A+v_B lnv_B)-\frac{1}{2}v_B(lnv_B)^2} \qquad (7)$$

where v_A and v_B are the volume fractions of dispersed and continuum phases, respectively. These will be assumed to correspond to the pore volume fractions occupied by entrapped mercury, and remaining vacant.

RESULTS

Basic Material Properties

Table 1 shows the basic characteristics of the two pellet samples studied. As might be anticipated, the porosity and specific surface area are lower for the high density sample. Figure 2 shows 2D slice CXT cross-sections of typical samples from each batch. The dark areas correspond to regions of low X-ray absorbance, while the bright white regions correspond to regions of denser material with greater X-ray absorbance. In the CXT image for the LD material it can be seen that there are irregular, spatially-extended regions of relatively high density surrounded by boundaries of relatively low density. This suggests that, for the LD sample, the CXT images reveal that the individual shapes and sizes of the feed particles for compaction are still distinguishable due to gaps or low density regions left at their contact zones, whereas these are much less evident for the HD sample. The pre-compaction process results in irregular-shaped particles that inter-lock in the tablet. The CXT images of the LD pellets in Figures 2(a)-(c) show cross-sections of constituent irregular-shaped particles with characteristic sizes in the range ~100-2000 μm. From Figure 2(d), it thus seems that the compaction to higher density creates a greater degree of merging of feed particles. It is also noted that many of the constituent particles of the LD pellet exhibit cracks through their central regions, or splintering off of smaller particles at their edges, which probably result from the distribution of stresses during the compaction process. These features have been largely closed up by the higher pelleting pressure in the HD pellets. Table 2 shows typical values of the reduced standard deviation in image pixel intensities for radial slice images of several different planes within a typical pellet taken from each batch. It can be seen that relative heterogeneity in porosity is generally larger for the LD pellets.

Table 1: Characteristics of samples studied. The bulk density and porosity were obtained from helium-mercury pycnometry.

Sample	**Bulk Density ($g\ cm^{-3}$)**	**Porosity (%)**	**BET Surface Area ($m^2\ g^{-1}$)**	**Cylinder Dimensions (base diameter × height)**
Low Density (LD)	1.93	55	89	5mm × 5mm
High Density (HD)	2.32	47	79	5mm × 3.5mm

Figure 2: CXT images of cross-sections through typical examples of cylindrical pellets of (a)-(c) LD and (d) HD samples. The scale bar corresponds to 1000 μm.

(a)

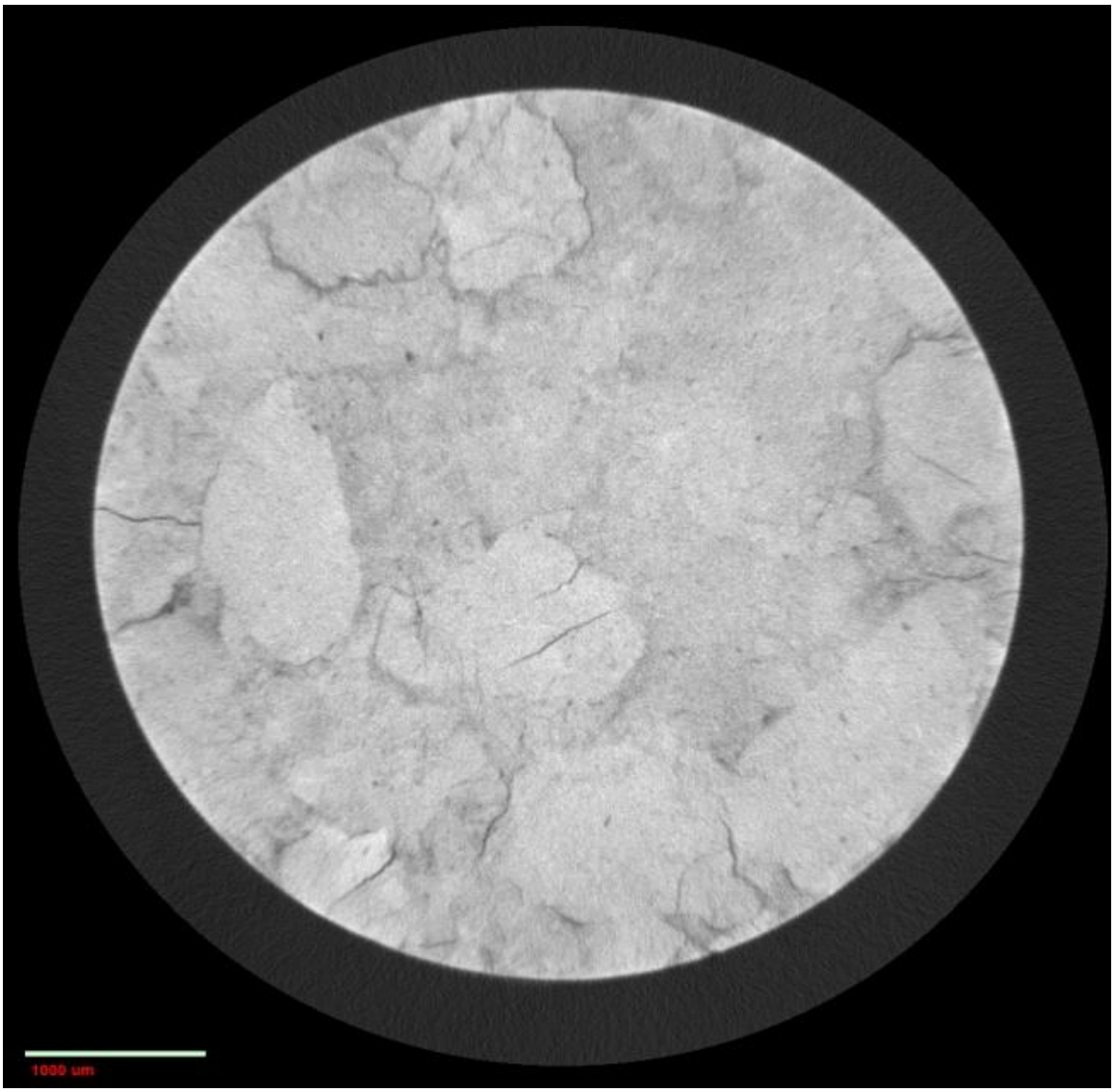

(b)

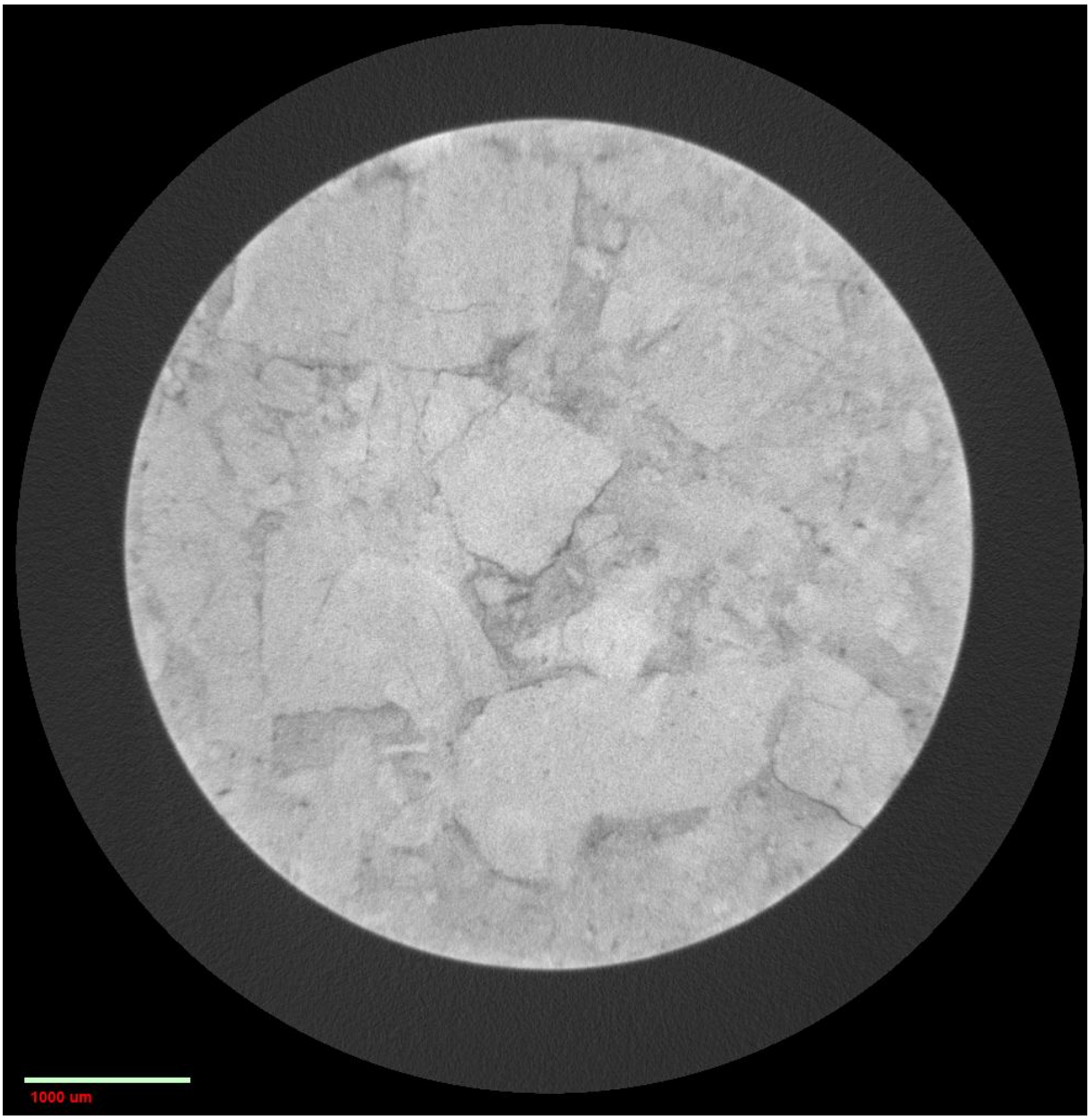

(c)

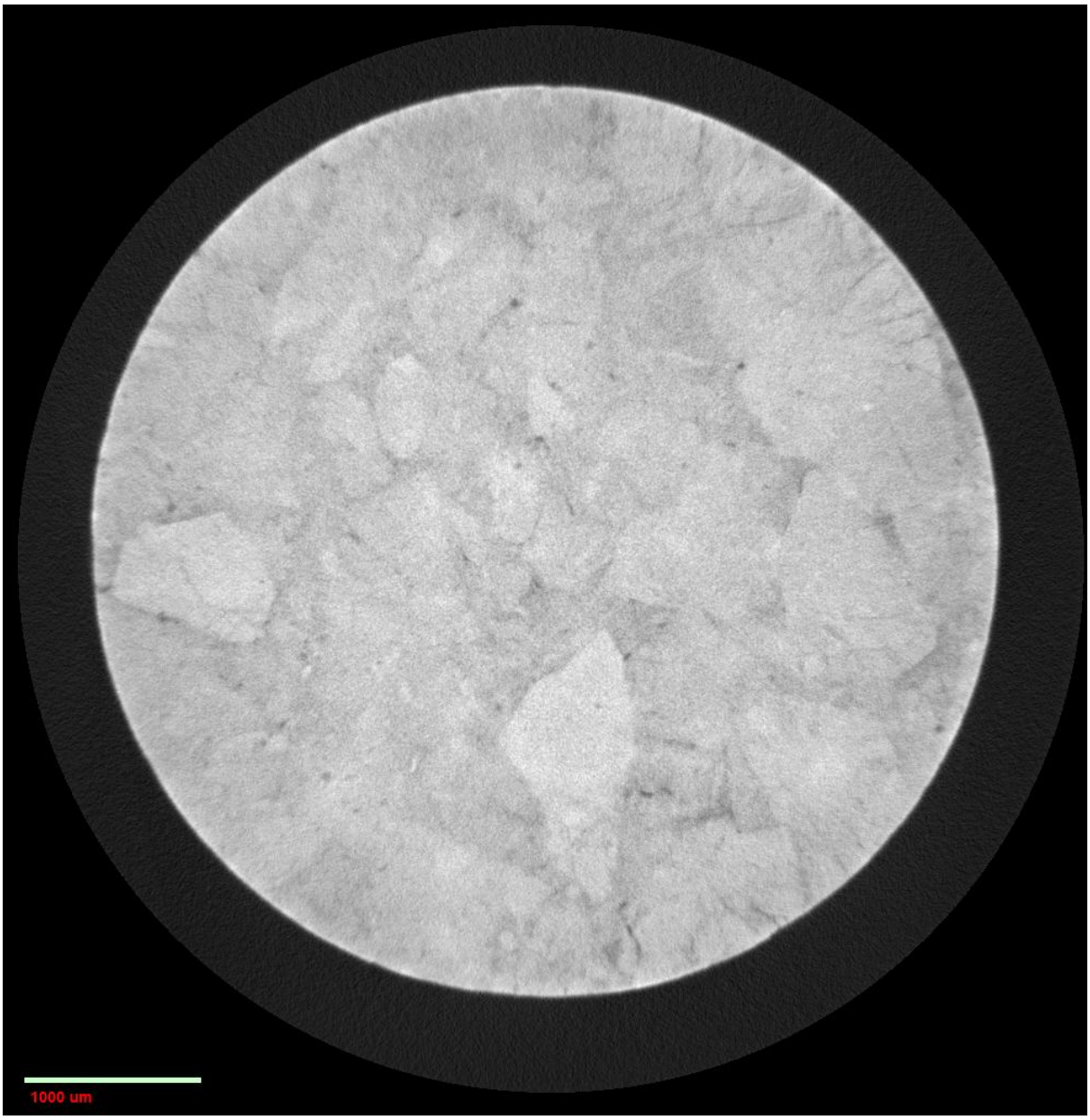

(d)

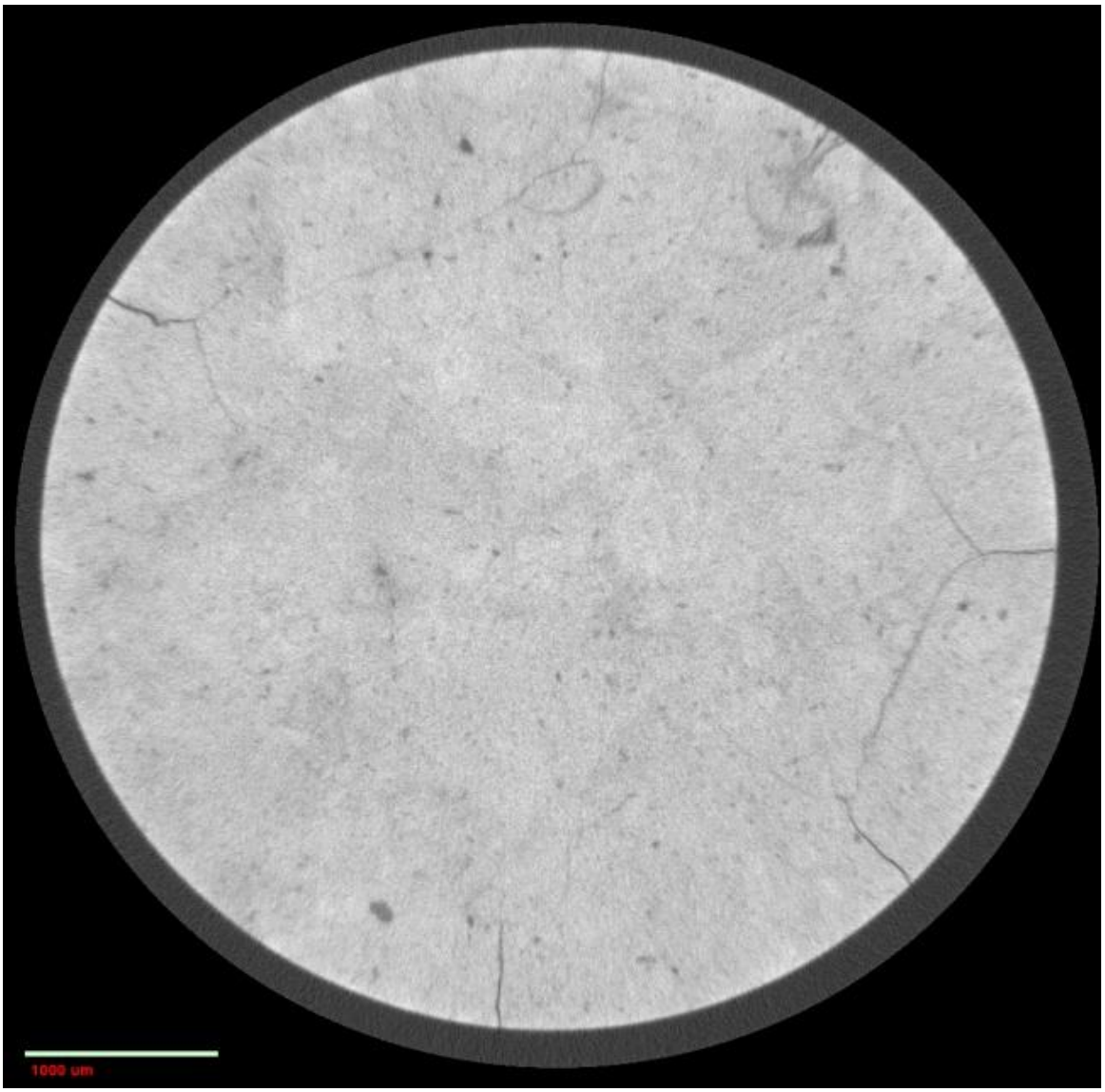

Table 2: Typical values of the reduced standard deviation in image pixel intensities for radial slice images of several different planes within a typical pellet taken from each batch.

Image set	LD Pellet #1	LD Pellet #2	HD Pellet #1	HD Pellet #2
Slice position				
400	0.0700	0.0770	0.0693	0.0693
500	0.0698	0.0863	0.0698	0.0665
600	0.0701	0.0830	0.0630	0.0644
700	0.0684	0.0726	0.0622	0.0623

Gas sorption and mercury porosimetry

Figures 3 and 4 show typical examples of gas sorption isotherms for fresh samples, and also for samples following mercury intrusion scanning curves to different pressures. The mercury porosimetry scanning curves involved intrusion to a range of ultimate pressures. Also shown in Figure 5 are the corresponding mercury porosimetry scanning curve data. It can be seen that, as more mercury becomes entrapped, the ultimate amount of gas adsorbed at the top of the isotherms decreases. The form of the sorption hysteresis loops is generally such that desorption begins immediately on reversal of pressure increases, except, perhaps for the HD pellets at the highest mercury entrapment levels. This behaviour is, normally, typical of sorption scanning curves where the void space is not completely filled with liquid nitrogen at the top of the isotherm, and pockets of vapour remain into which condensate can immediately begin to evaporate (Rouquerol *et al.*, 1999).

Figure 3: Typical examples of gas sorption isotherms for fresh samples, and samples following mercury intrusion scanning curves to different pressures (solid line, fresh; short dash line, 31.5 MPa; long dash-space line, 117 MPa; dash-dot line, 227 MPa) of LD pellets.

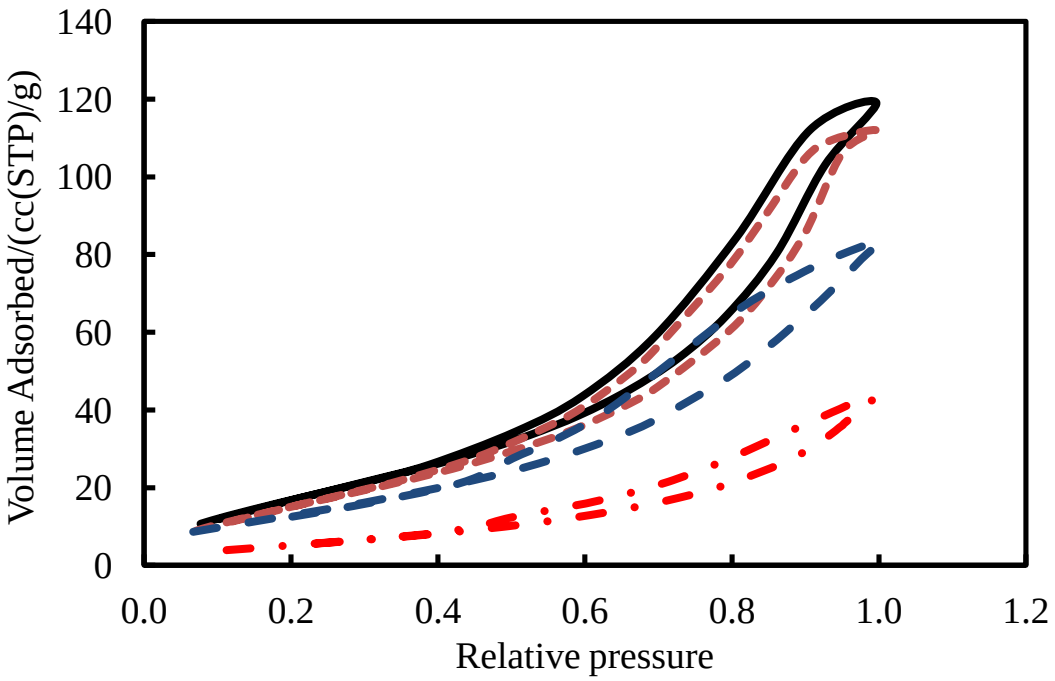

Figure 4: Typical examples of gas sorption isotherms for fresh samples, and samples following mercury intrusion scanning curves to different pressures (solid line, fresh; short dash line, 75.7 MPa; long dash-space line, 103 MPa; dash-dot line, 159 MPa; two dot-dash, 227 MPa) of HD pellets.

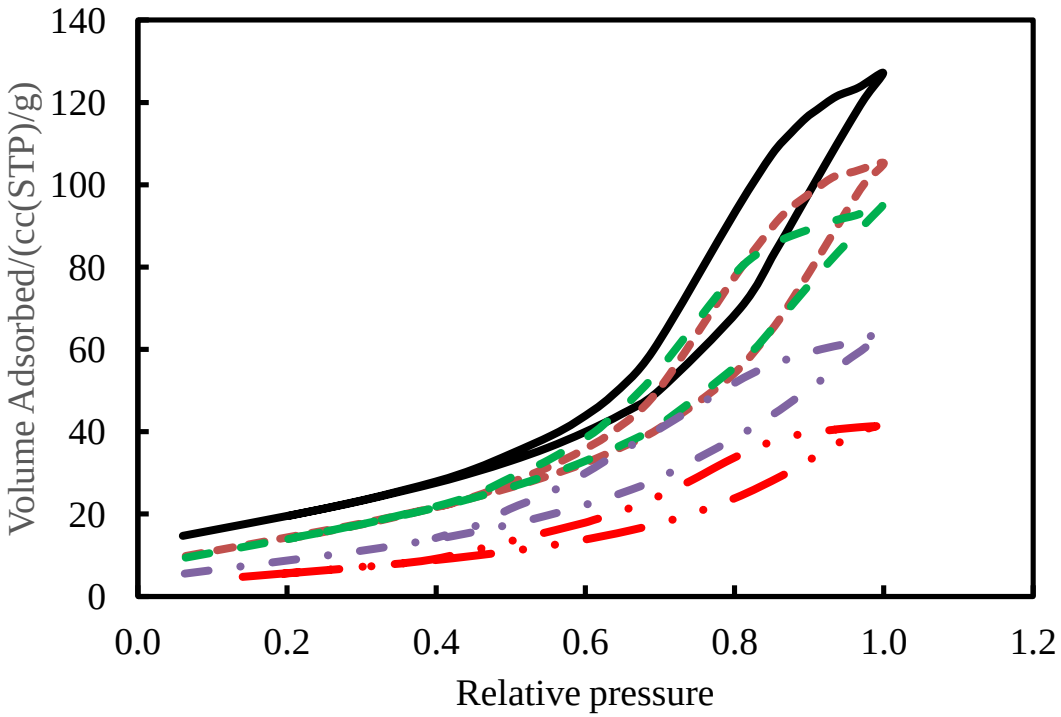

Figure 5: Typical examples of mercury porosimetry scanning curves to various ultimate pressures indicated in legend for (a) LD and (b) HD samples.

(a)

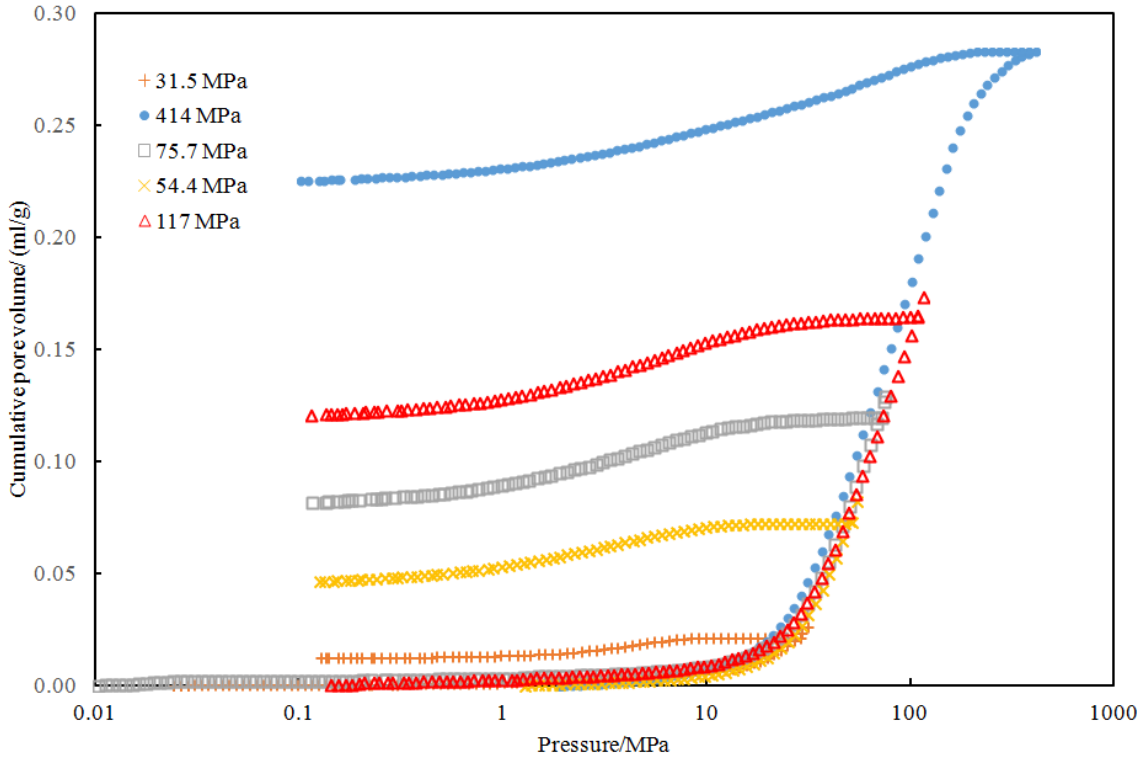

(b)

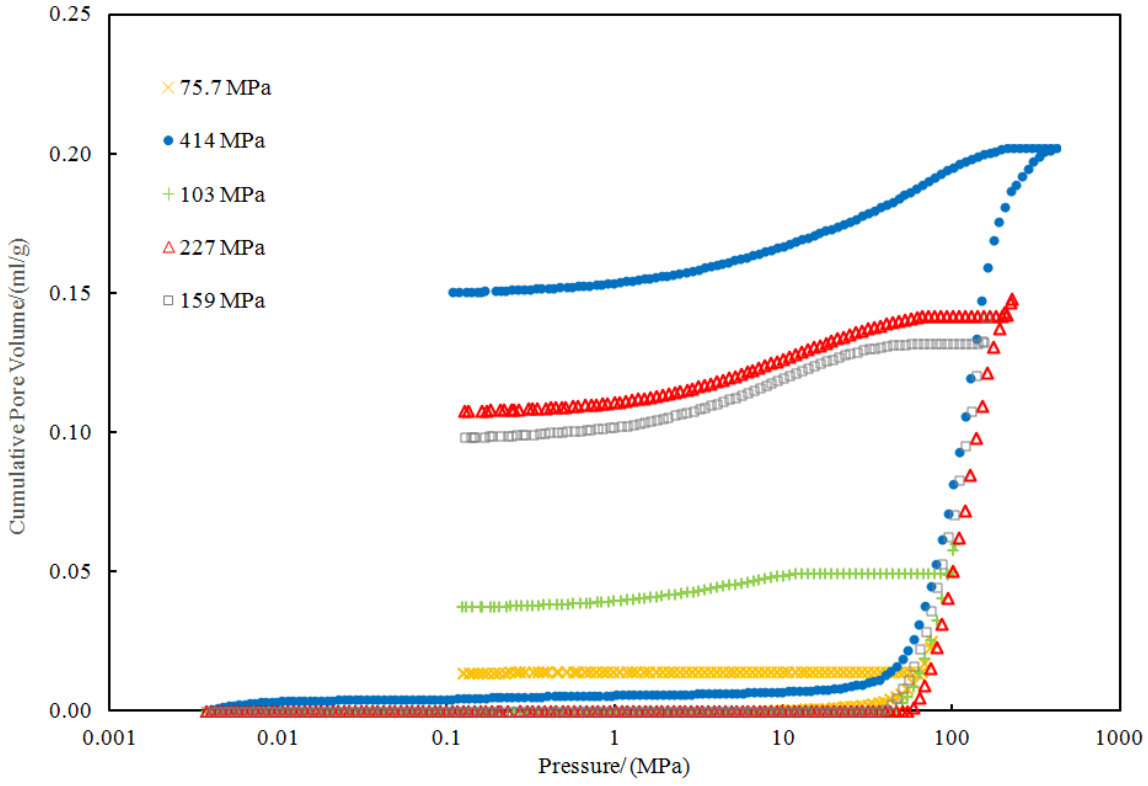

Table 3 shows the specific pore volumes determined from gas adsorption (Gurvitch volume), mercury intrusion, and helium pycnometry. It can be seen that the sample mean pore volumes from gas sorption and mercury porosimetry are less than that for helium pycnometry, albeit close for porosimetry. This suggests that there are pores too large to achieve condensation of nitrogen within, and pores shielded by necks too small for mercury to enter.

Table 3: Specific pore volume, determined by three different methods, and modal pore size, determined by two methods, for the LD and HD samples.

Sample	**Mercury porosimetry pore volume /(ml/g)**	**Nitrogen sorption pore volume /(ml/g)**	**Helium pyconometry pore volume /(ml/g)**	**Mercury porosimetry modal pore radius /nm**	**Nitrogen sorption modal pore radius /nm**
LD	0.28 ±0.02	0.22±0.02	0.30±0.02	8.1	7.3
HD	0.20±0.02	0.199±0.003	0.21±0.02	5.3	6.5

Figure 6 shows a comparison of the cumulative pore size distributions obtained from BJH analysis of the nitrogen adsorption isotherm and the mercury porosimetry intrusion curve, using the Kloubek correlations (1981), for the LD and HD fresh samples. Table 3 shows the modal pore sizes determined from these distributions for each type of sample. It can be seen that for both samples the modal pore size determined from each method is within ~1 nm of each other. However, the width of the mercury intrusion PSD is generally narrower than for that from gas sorption, even allowing for the lower limit on pore size probed by porosimetry.

Figure 6: Cumulative PSDs determined from mercury porosimetry (solid line) and nitrogen adsorption (dashed line) for (a) LD and (b) HD fresh samples.

(a)

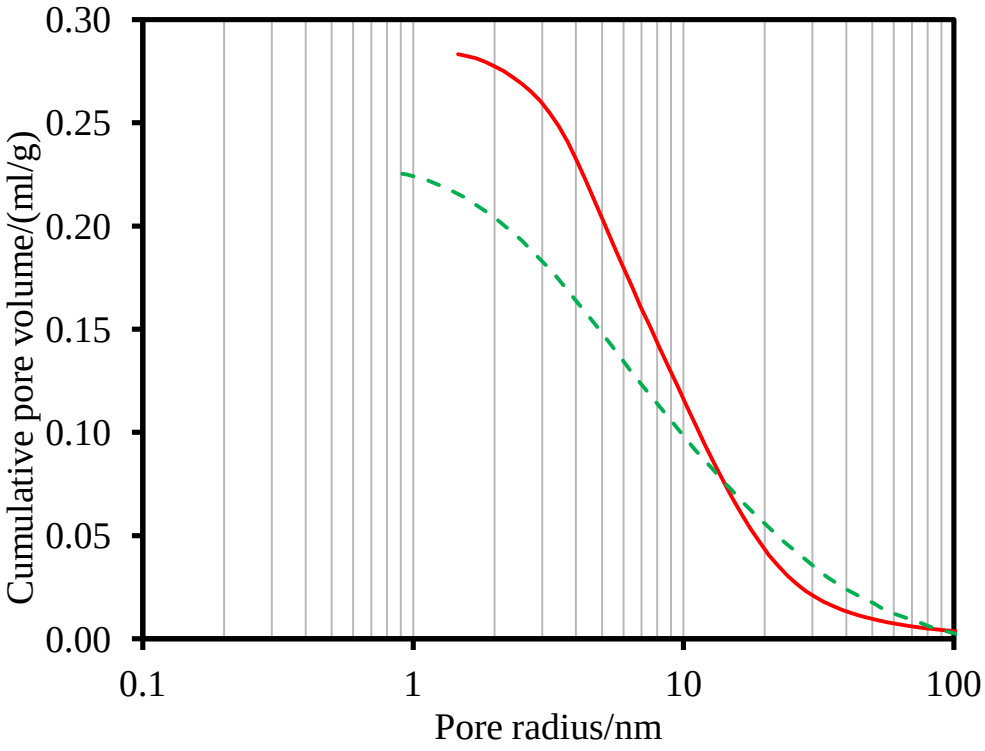

(b)

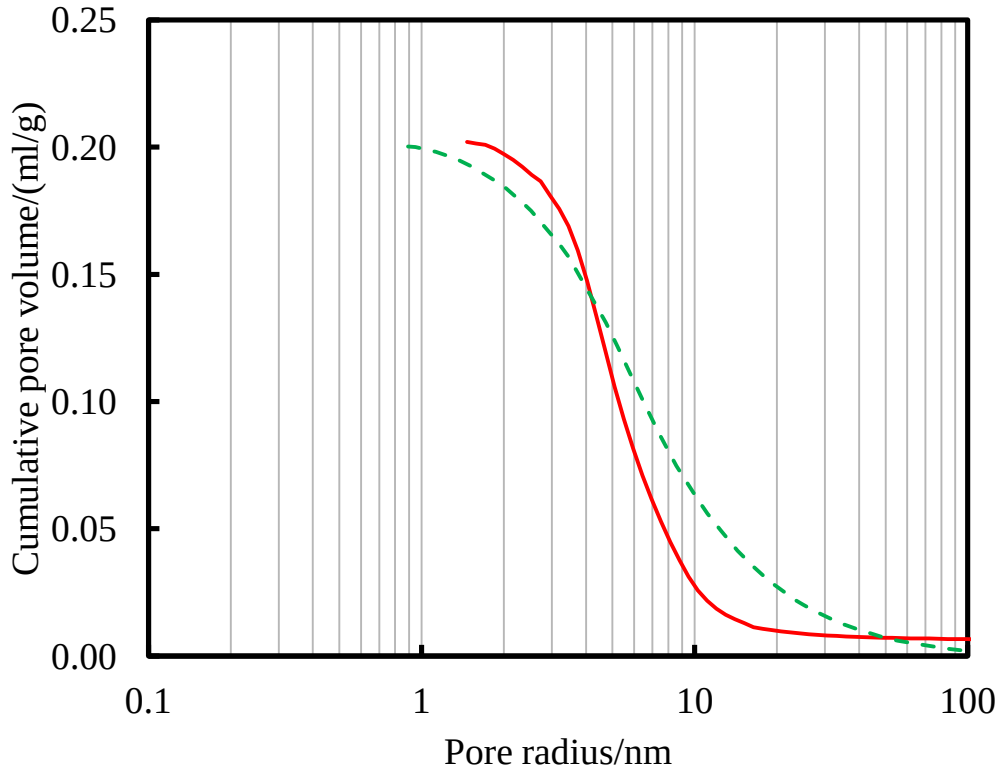

Structure-transport relationship for LD pellets

Table 4 shows the variation in adsorption-corrected mtc, for the LD sample, with fraction of pore volume occupied by mercury, and a comparison with that expected for a completely random arrangement of entrapped mercury, as predicted by the Prager (1960) model. Each mtc is expressed as a ratio to the mtc for the mercury-free sample, denoted k_0. From Table 4 it can be seen that, for the case with 16% of the pore volume filled with mercury, the mtc declines significantly less than expected for a random arrangement of mercury. This may suggest that the pores filled with mercury are of relatively low importance for mass transport. The increase in the mtc, even above the original value for the empty sample, for the sample with 29 % of the void space filled with mercury suggests that the effective characteristic particle size has been reduced.

Table 4: The variation in adsorption-corrected mtc, for the LD sample, with fraction of pore volume occupied by mercury, and a comparison with that expected for a completely random arrangement of entrapped mercury, as predicted by the Prager (1960) model. Each mtc is expressed as a ratio to the mtc for the mercury-free sample, denoted k_0 (=0.037±0.004 s^{-1}). The quoted errors reflect intra-batch variability.

Minimum pore radius penetrated/nm	**Pore volume fraction containing mercury/%%**	**Experimental k/k_0**	**Expected k/k_0 for random arrangement of mercury (Prager)**
(Fresh sample)	0	1.0	1.0
11	16	0.89±0.02	0.70 ±0.02
8	29	1.62±0.18	0.65±0.02

Figure 7 shows the gas adsorption size distributions of the particular subsets of pores that are being blocked from external accessibility by progressively higher pressure porosimetry scanning curves for the LD sample. These difference distributions are obtained by subtracting the gas adsorption pore size distributions obtained from isotherms for samples following successive mercury scanning curves. It can be seen that large (~15 nm) and medium (~10 nm) pores are blocked initially, following the lower pressure scanning curves, while the

scanning curve to highest pressure shown fills some remaining medium-sized pores and also begins to fill the smallest pores of ~3-4 nm. Hence, access to pores is generally declining with size as intrusion pressure is increased, as might be expected. The integrated nitrogen adsorption data is sensitive to pore body size. This thus also revealed that some large pores are still filling at the highest pressure as they have been shielded by smaller pore necks. The shielding necks will affect accessibility of the largest pores and thus their transport effectiveness. Experiments were also conducted for the very highest ultimate intrusion pressures shown in Figure 5 but the externally accessible void space volume was then very low so the data is not shown in Figure 7.

Figure 7: Gas adsorption size distributions for the particular subsets of pores that are being blocked from external accessibility by progressively higher pressure (as indicated) porosimetry scanning curves for LD sample.

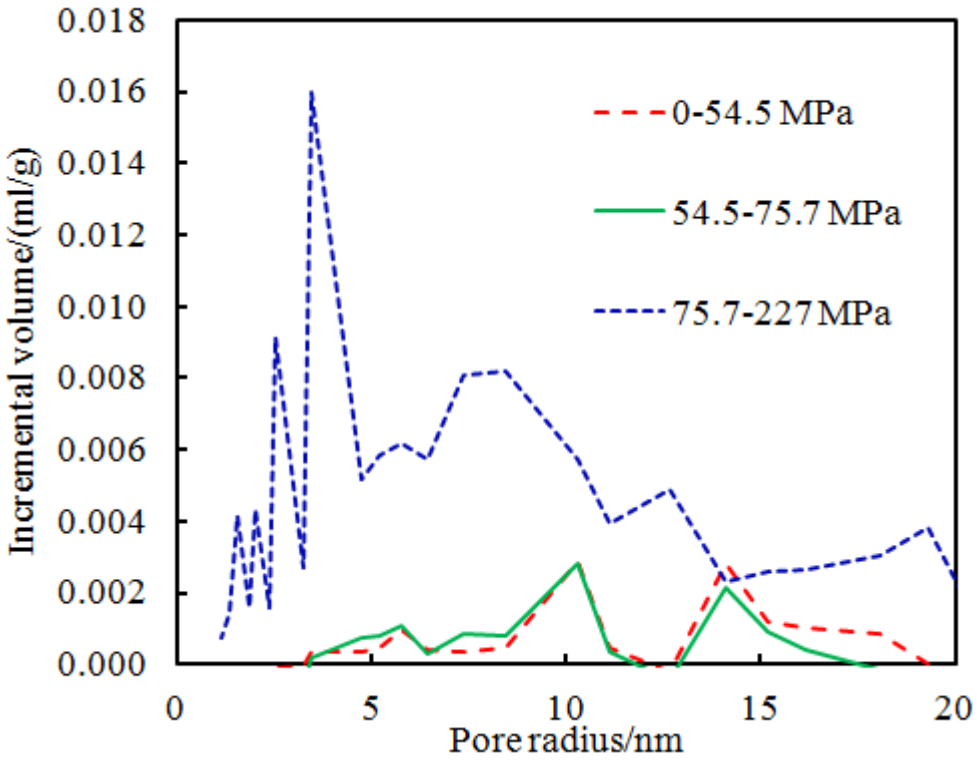

Figure 8 shows CXT images of typical radial slices through LD pellets, and a reconstructed view of the pellet exterior, following mercury porosimetry leading to entrapment filling 16% of the void space. The brightest white pixel intensities are associated with entrapped mercury because they represent the largest X-ray absorbance, and mercury is by far the heaviest

element present in the samples. It can be seen that mercury is predominantly filling the long and slender, or sheet-like, void spaces between feed particles and/or cracks in the pellet.

Figure 8: (a-c) CXT images of typical radial slices through LD pellets, and (d) a reconstructed view of the pellet exterior, following mercury porosimetry leading to entrapment filling 16% of the void space. Bright white regions correspond to high electron density, and thus mercury. The lower left scale bars correspond to 1000 μm.

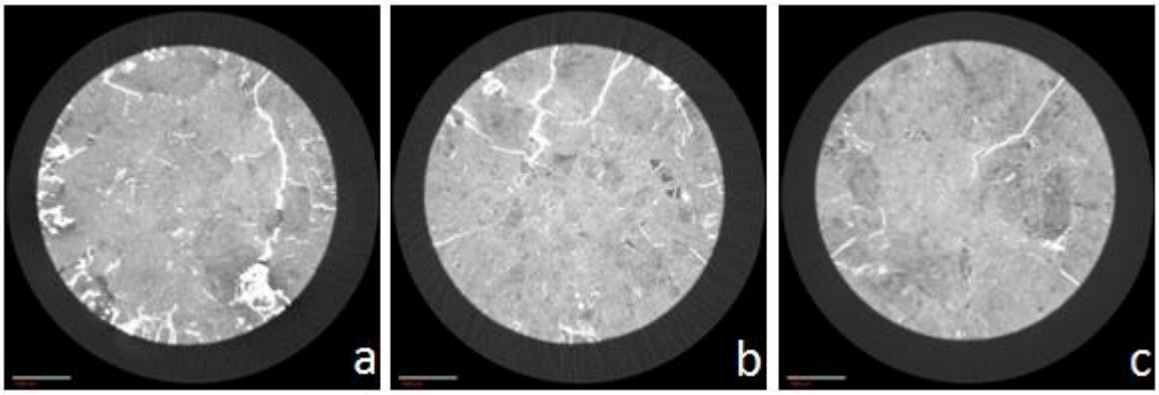

(d)

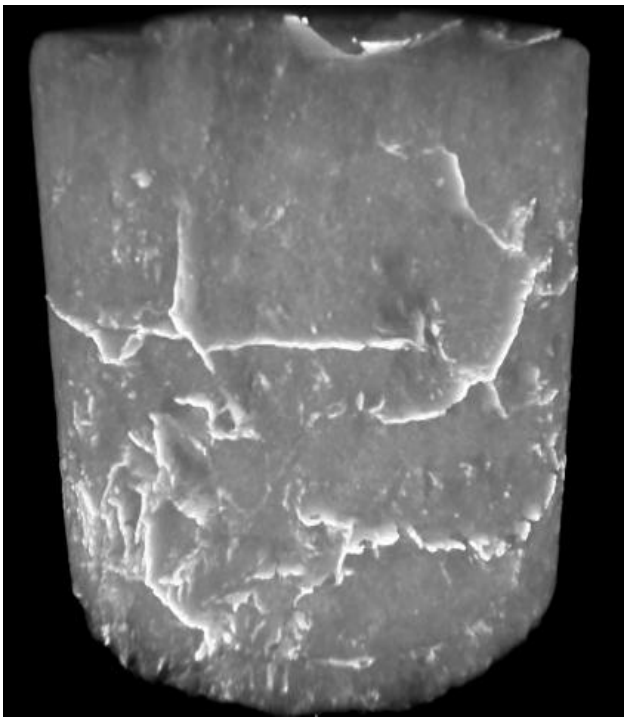

Figure 9 shows examples of radial slices through LD pellets following filling of 29 % of the void space with entrapped mercury. It can be seen that well-defined aspects of the mercury entrapment pattern often follow the envelope surrounding pellet feed particles. The concentration of the entrapment in these regions may be due to the increased pore space heterogeneity created at the feed particle margin due to splintering during compaction. It is also noted that more hazy patches of mercury entrapment are now also appearing within feed particle regions, and there may be some concentration of this entrapment towards the centre core zone of the pellet. If entrapped mercury completely fills porosity towards the centre of the pellet, or forms a complete shell around a feed particle near the centre of the pellet, this would act to reduce the effective characteristic particle size, and result in a rise in observed mtc.

Figure 9: Examples of radial slices through typical LD pellets following filling of 29 % of the void space with entrapped mercury. The scale bar corresponds to 1000 μm.

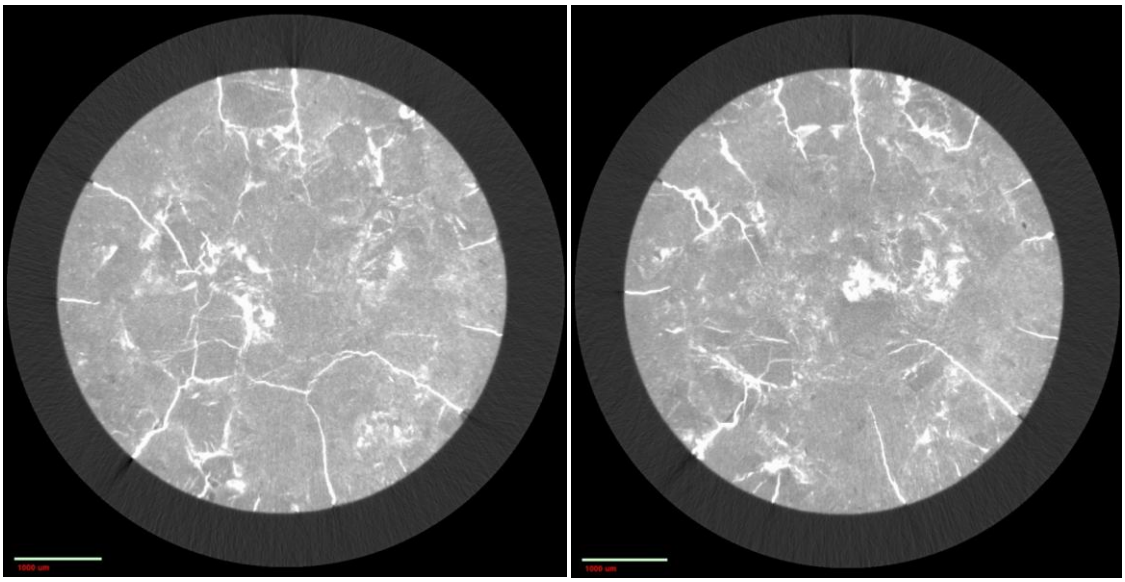

Structure-transport relationship for HD pellets

Table 5 shows the variation in adsorption-corrected mtc, for the HD sample, with fraction of pore volume occupied by mercury, and a comparison with that expected for a completely random arrangement of entrapped mercury, as predicted by the Prager (1960) model. For a sample with 6.8 % of the void volume filled with entrapped mercury, the mtc is much lower than that expected for a random arrangement of mercury, thereby suggesting that the pores

filled with mercury must have been making a significant contribution to mass transport. However, for the sample with 18.5 % of void volume filled with mercury, the observed mtc is then in-line with what would be expected for a random arrangement of entrapped mercury. Further, for the sample with 53.5 % of void volume filled with entrapped mercury, the mtc is larger than would be expected for a random arrangement of mercury, suggesting that the pores filled with mercury by the final scanning loop are less important to mass transport than they would have been if they had been distributed more randomly, and thus more homogeneously. A non-random arrangement could also decrease effective characteristic particle size.

Table 5: The variation in adsorption-corrected mtc, for the HD sample, with fraction of pore volume occupied by mercury, and a comparison with that expected for a completely random arrangement of entrapped mercury, as predicted by the Prager (1960) model. The quoted errors reflect intra-batch variability. k_0 = 0.035±0.003 s^{-1}.

Minimum pore radius penetrated/nm	**Pore volume fraction containing mercury/%%**	**Experimental k/k_0**	**Expected k/k_0 for random arrangement of mercury (Prager)**
(Fresh sample)	0	1.0	1.0
8.0	6.8	0.515±0.001	0.911 ±0.001
5.9	18.5	0.758±0.001	0.764±0.001
2.7	53.5	0.636±0.001	0.378±0.001

Figure 10 shows the pore size distributions for the sub-sets of pores that progressively become inaccessible from the exterior as the mercury entrapment is increased. It is noted that the steep decline in incremental volume at the lowest pore size present in each distribution corresponds to the minimum penetrated radius of ~8, ~6, or ~3 nm, for ultimate mercury intrusion pressures of 75.7, 103 or 227 MPa, respectively. This suggests that the BJH pore size obtained is similar to that obtained using the Kloubek (1981) correlation for mercury intrusion, in this case. From Figure 10, it can be seen that, at low levels of mercury entrapment, access to pores of sizes in the range ~10-20 nm is lost, while for higher levels of

mercury entrapment access is lost to pores of sizes ~6-10 nm. Hence, access to pores is generally declining with size as intrusion pressure is increased, as might be expected.

Figure 10: Gas adsorption pore size distributions for the sub-sets of pores that progressively become inaccessible from the exterior as the mercury entrapment is increased for progressively higher ultimate pressures (as indicated in legend) for scanning curves.

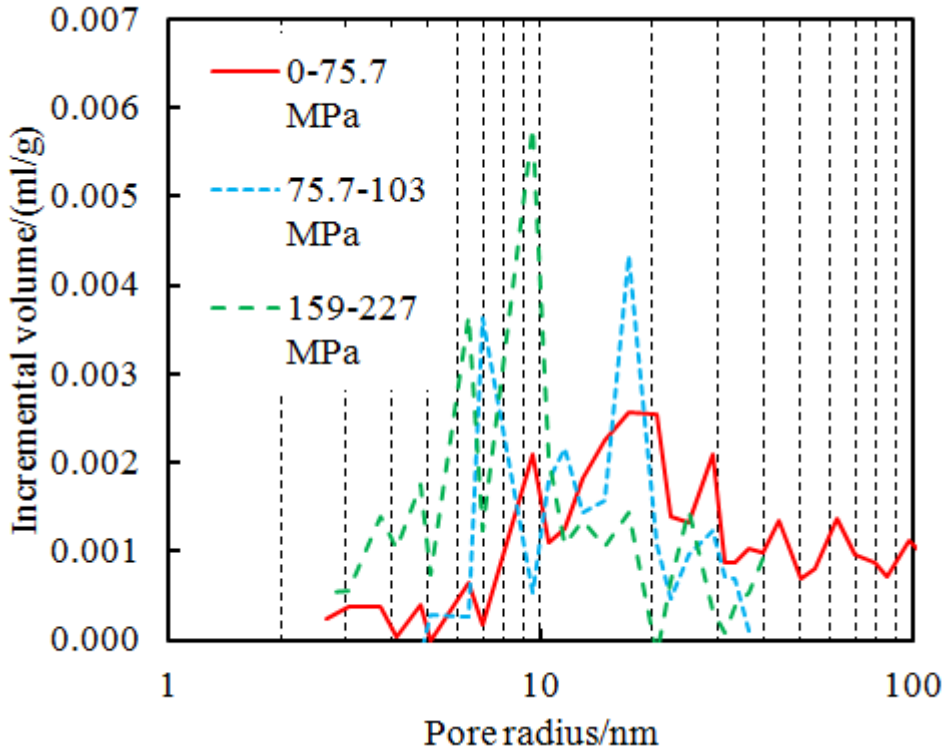

Figure 11 shows CXT images of typical radial slices through HD pellets following mercury porosimetry leading to entrapment filling 6.8 % of the void space. Once again, the brightest white pixel intensities are associated with entrapped mercury. It can be seen that the majority of the entrapped mercury is associated with long slender regions extending from the pellet surface to a depth of about one quarter of the pellet diameter, though there are also isolated regions of entrapped mercury closer to the pellet centre. It is noted that there are regions of the images that are very dark in voxel intensity and, thus, correspond to probably very little, or no, entrapped mercury, suggesting a heterogeneous distribution. Figure 12 shows CXT images of typical radial slices through HD pellets following mercury porosimetry leading to entrapment filling 18.5 % of the void space. It can be seen that some entrapped mercury 'coronae' surrounding irregular patches in the image have started to appear, though not in as

substantial numbers as for the LD pellet. However, there are also more isolated regions of mercury within still identifiable patches in pellet density. Overall, the bright white voxels corresponding to high X-ray absorbance seem more pervasively distributed than for Figure 11, and also compared with the images of the LD pellets for a similar mercury saturation.

Figure 11: CXT images of typical radial slices through HD pellets following mercury porosimetry leading to entrapment filling 6.8 % of the void space. The scale bar corresponds to 1000 μm.

(a) (b)

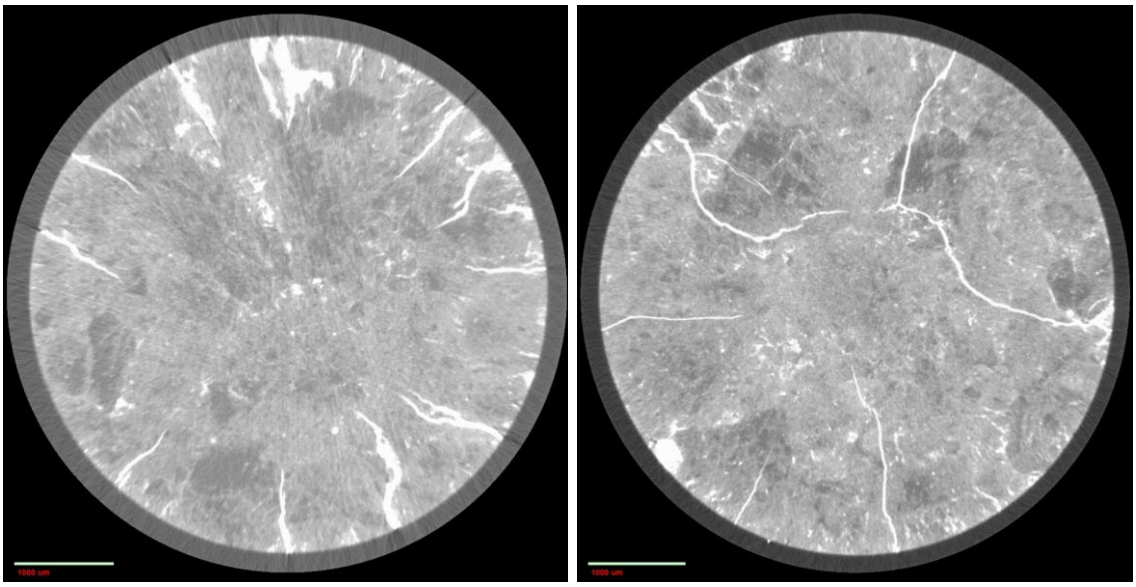

Figure 12: CXT images of typical radial slices through HD pellets following mercury porosimetry leading to entrapment filling 18.5 % of the void space. The scale bar corresponds to 1000 μm.

(a) (b)

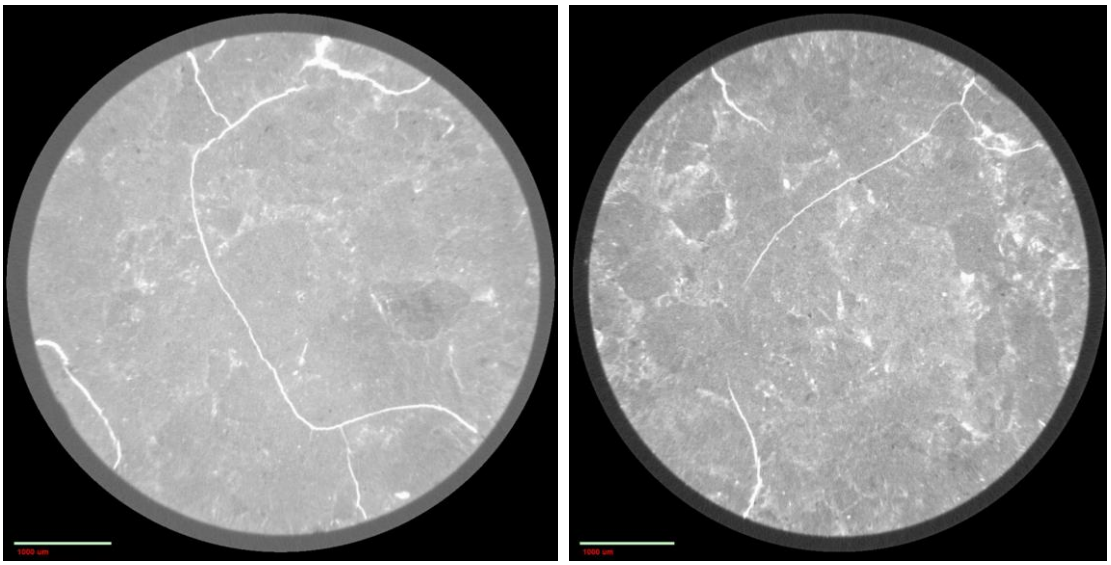

DISCUSSION

It has been observed above that the loss of the largest pore sizes (following mercury penetration of pore sizes down to 8 nm radius) had the opposite effect on the mtc in LD and HD pellets. For LD pellets, the mtc declined less relative to that expected for the random case, while, for HD pellets, the mtc declined more relative to that expected for the random case. There was a difference in the overall level of mercury entrapment after intrusion of pores down to 8 nm, with 29 % of the pore volume containing mercury in LD pellets and 6.8 % in HD pellets.

However, when similar fractions of the pore volume of each type of pellet were filled with entrapped mercury (similar mercury saturation), there was also a difference between the relative decline of the mtc. With 18.5 % of the void volume of the HD pellets filled with mercury, the decline in the observed mtc was well predicted by the random Prager (1960) model, but, for the LD pellet, when 16 % of the void space was filled with mercury, the observed mtc was significantly higher than expected from the random model. This latter result suggests the mercury distribution is probably more spatially correlated than for the random case and is located in regions with relatively less importance for mass transport.

The CXT data has demonstrated significant observable differences in the spatial distribution patterns of entrapped mercury. For the LD pellet entrapment seems to be relatively more concentrated in the boundary regions between pellet feed particles, while for HD pellets the mercury is also more commonly found in regions elsewhere. This more homogeneous distribution of mercury is consistent with the better success of the random (and thus macroscopically homogeneous) Prager (1960) model in predicting the mtc. This difference in location of entrapment is due to compaction pressure difference.

CONCLUSIONS

It has been demonstrated that the new integrated gas ROA and porosimetry experiment, coupled with complementary CXT data, can deliver novel and comprehensive information on the transport effectiveness of different sets of pores within porous pellets, and their likely origins. It has been observed, from the CXT images, that, at the lower compaction pressure used to make the LD pellets, many more residual regions of low density and cracks were left surrounding the constituent feed particles compared with the HD pellets. The more macroscopically homogeneous structure of the HD pellet meant that pore sizes were more evenly distributed across the sample, such that the mass transport model assuming a random distribution of entrapped mercury was more successful in predicting the impact of the mercury on mass transport. This heterogeneity has also meant that the largest pores present in each system have differences in relative importance of contribution to mass transport. The largest pores in the LD sample were found to make a contribution lower than might be anticipated. The CXT images suggested that this is because of the lack of pervasiveness of these pores.

ACKNOWLEDGEMENTS

SPR and AN are grateful to Johnson Matthey plc and the Engineering and Physical Sciences Research Council (EPSRC) of the UK for the award of a CASE PhD studentship.

REFERENCES

Barrett, E.P., Joyner, L.G., & Halenda, P.H. (1951). The Determination of Pore Volume and Area Distributions in Porous Substances. I. Computations from Nitrogen Isotherms. *Journal of the American Chemical Society* 73, 373-380.

Crank, J. *The Mathematics of Diffusion* (2nd edn.). Oxford: Clarendon Press, 1975.

Do D. *Adsorption Analysis: Equilibria and Kinetics*. London: Imperial College Press, 1998.

Giacobbe, F.; Aylmore, L.A.G.; Steele, W.A. (1972). Thermodynamic properties of argon adsorbed on porous glass plus preadsorbed water, *Journal of Colloid Interface Science* 38 277-284.

Gopinathan, N., Greaves, M., Wood, J., Rigby, S.P. (2013). Investigation of the problems with using gas adsorption to probe catalyst pore structure evolution during coking, *Journal of Colloid Interface Science* 393, 234–240.

Hitchcock, I., Chudek, J.A., Holt, E.M., Lowe, J.P., Rigby, S.P., (2010). NMR Studies of Cooperative Effects in Adsorption, *Langmuir* 26, 18061-18070.

Hitchcock, I., Holt, E.M., Lowe, J.P., Rigby, S.P., (2011). Studies of freezing-melting hysteresis in cryoporometry scanning loop experiments using NMR diffusometry and relaxometry, *Chemical Engineering Science* 66, 582-592.

Hitchcock, I., Lunel, M., Bakalis, S., Fletcher, R.S., Holt, E.M., Rigby, S.P. (2014). Improving sensitivity and accuracy of pore structural characterisation using scanning curves in integrated gas sorption and mercury porosimetry experiments, *Journal of Colloid Interface Science* 417, 88-99

Hollewand, M.P., and Gladden, L.F., (1993). Heterogeneities in structure and diffusion within porous catalyst support pellets observed by NMR imaging, *Journal of Catalysis* 144, 254-272.

Hollewand, M.P., and Gladden, L.F., (1995). Transport heterogeneity in porous pellets-II. NMR imaging studies under transient and steady-state conditions, *Chemical Engineering Science* 50, 327-344.

Holzer, L., Indutnyi, F., Gasser, P.H., Munch, B., Wegmann, M. (2004) Three-dimensional analysis of porous BaTiO3 ceramics using FIB nanotomography, *Journal of Microscopy* 216, 84-95.

Hyväluoma, J., Raiskinmäki, P., Jäsberg, A., Koponen, A., Kataja, M., and Timonen J., (2004). Evaluation of a lattice-Boltzmann method for mercury intrusion porosimetry simulations, *Future Generations Computer Systems* 20, 1003-1011.

Kloubek, J., (1981). Hysteresis in porosimetry, *Powder Technology* 29, 63-73.

Koster, A.J., Ziese, U., Verklejj, A.J., Janssen, A.H., and De Jong, K.P., (2000). Three-dimensional transmission electron microscopy: a novel imaging and characterization technique with nanometre scale resolution for materials science, *Journal of Physical Chemistry B* 104, 9368-9370.

Morishige, K.; Kanzaki, Y. (2009). Porous Structure of Ordered Silica with Cagelike Pores Examined by Successive Adsorption of Water and Nitrogen , *Journal of Physical Chemistry C* 113, 14927-14934.

Pavlovskaya, G. ; Six, J., Meersman, T., Gopinathan, N., Rigby, S.P. (2015). NMR Imaging of Low Pressure, Gas-Phase Transport in Packed Beds Using Hyperpolarized Xenon-129 *AIChEJ* 61, 4013-4019.

Prager, S. (1960). Diffusion in Inhomogeneous Media, *Journal of Chemical Physics* 33, 122-127.

Rigby, S.P., Chigada, P.I., Wang, J., Wilkinson, S.K., Bateman, H., Al-Duri, B., Wood, J., Bakalis, S., Miri, T., (2011). Improving the Interpretation of Mercury Porosimetry Data using Computerised X-ray Tomography and Mean-Field DFT, *Chemical Engineering Science* 66, 2328-2339.

Rigby, S.P., Fletcher, R.S., Riley, S.N., (2004). Characterisation of porous solids using integrated nitrogen sorption and mercury porosimetry. *Chemical Engineering Science* 59, 41-51.

Rouquerol, F., Rouquerol, J., Sing, K., *Adsorption by Powders and Porous Solids: Principles, Methodology and Applications*; Academic Press: London, 1999.

Strange, J.H. and Webber, J.B.W. (1997). Spatially resolved pore size distributions by NMR, *Measurement Science & Technology* 8, 555-561.

Wardlaw N.C., McKellar M., (1981). Mercury porosimetry and the interpretation of pore geometry in sedimentary rocks and artificial models. *Powder Technology* 29, 127-143